

# Radiative transfer effects in hydrogen recombination masers

C. Hengel and W.H. Kegel

Institut für Theoretische Physik der Universität Frankfurt am Main, Robert-Mayer-Strasse 10, 60054 Frankfurt, Germany

Received 7 April 2000 / Accepted 10 July 2000

**Abstract.** Using a simple on-the-spot approximation, we explore the parameter range in the  $(\log(R), \log(n_e))$  plane for which maser action in atomic hydrogen is present and briefly discuss how the borderlines of this region of strong population inversion arise. In particular we address the influence of radiative transfer on the population structure. We find that in normal HII regions no strong maser activity occurs, while for ultra compact HII regions in a certain parameter range strong hydrogen masers should be found. Our fit to the available observational data for MWC 349 leads to a density estimate that is compatible with previous work (Thum & Greve 1997). Furthermore, we derive for the first time a reasonable representation of the variation of the flux ratio of  $Hn\beta$  and  $Hn\alpha$  lines measured towards MWC 349.

**Key words:** masers – radiative transfer – stars: individual: MWC 349 – stars: circumstellar matter – ISM: H II regions

## 1. Introduction

Calculations of the level populations of atomic hydrogen are not a new field in astronomical research. Extensive tables of the hydrogen population numbers and the corresponding emission coefficients have been supplied by various authors such as Storey & Hummer (1995) or Walmsley (1990). These calculations exclusively deal with the two standard cases of classical recombination line theory. Both of them, Case A and Case B, are good representations of an optically thin HII-region, being optically thin in the Lyman lines for Case A and optically thick in the Lyman lines for Case B. The discovery of a high density hydrogen recombination line maser in the circumstellar disk of MWC 349 (Martín-Pintado et al. 1989) has drawn new attention to the importance of radiative transfer for reliable predictions of optical depths and line intensities under extreme physical conditions. Strel'nitski et al. (1996) made an attempt to correct the present optically thin models for the influence of finite optical depths, but their method does not treat radiative transfer and statistical balancing self-consistently. Our intention was on the one hand to learn about the fundamental effect of radiative transfer on the population numbers of hydrogen under maser conditions and on the other hand to find a rough outline of the parameters for which maser action is to be expected. These aims require a

model that allows a self-consistent treatment of radiative transfer and rate equations. In order to avoid a misleading amount of parameters and to deal with the numerical problems arising from the presence of strong maser lines, we apply a simple on-the-spot approximation, which is an escape-probability-method with  $\beta_{ij} = e^{-\tau_{ij}}$ , similar to the one described e.g. by Köppen & Kegel (1980), Chandra et al. (1984), or Kegel (1979).

## 2. Theoretical concept and method of solution

### 2.1. Basic equations

The hydrogen population numbers are controlled by the set of statistical equations that describe the gain and loss rates of the number density of each energy level. In principle, each energy level  $i$  is split into  $i$  sublevels of angular momentum, each of them obeying an own rate equation. The results of Storey & Hummer (1995) show that especially for low densities this subdivision of the energy levels cannot be neglected when calculating the population numbers. However, the emphasis of this paper is on the influence of radiative transfer on the level population structure of rather compact and dense objects. If the electron density is less than  $10^6 \text{ cm}^{-3}$ , for an HII-region smaller than  $10^{15} \text{ cm}$  in diameter, the column density of neutral hydrogen will be too small for the stimulated radiative transitions to be of importance. With increasing electron density, the influence of the angular momentum substructure drops rapidly due to collisional redistribution. Hence, for our purpose it is admissible to neglect the angular momentum structure. The statistical equation for a given level  $i$  reads

$$\begin{aligned} \frac{dn_i}{dt} = & \sum_{j \neq i} n_j \left( A_{ij} + \frac{4\pi}{c} B_{ij} \tilde{J}_{ij} + C_{ij} \right) \\ & - n_i \sum_{j \neq i} \left( A_{ji} + \frac{4\pi}{c} B_{ji} \tilde{J}_{ji} + C_{ji} \right) \\ & - n_i (n_e q_{coll}(i) + q_{ph}(i)) \\ & + \alpha_i(T) n_e n_p + \phi_i(T) n_e^2 n_p, \end{aligned} \quad (1)$$

where

$$\tilde{J}_{ji} = \frac{1}{4\pi} \int \int I_{ij}(\nu, \Omega) \phi(\nu) d\Omega d\nu. \quad (2)$$

The  $C_{ij}$  are the probabilities for energy-changing collisional transitions from level  $j \rightarrow i$ , while the  $A_{ij}$ ,  $B_{ij}$  and  $B_{ji}$  denote

the Einstein coefficients for spontaneous and stimulated emission and absorption, respectively (for  $j < i$  we have  $A_{ij} = 0$ ). The  $q_{coll}(i)$  and  $q_{ph}(i)$  are the rate coefficients for collisional ionization and photoionization, and the  $\alpha_i(T)$  and  $\phi_i(T)$  represent two- and three-body recombination respectively. As we do not adopt standard Case B conditions, we also have to consider the population of the ground state. The ground state population is essentially controlled by the processes governing the ionization equilibrium. If these processes are well known the appropriate procedure is to replace the statistical equation for the ground state by the ionization balancing equation. If however the ionizing radiation field is not well known, as in the case of MWC 349, the ground state statistical equation should rather be replaced by a normalization equation, fixing the degree of ionization to a reasonable value. The value we use is  $n_{HI}/n_e = 10^{-4}$ .

By the terms containing the angle and profile averaged line intensities  $\tilde{J}_{ij}$ , the set of rate equations is non-linearly coupled to the solution of the corresponding radiative transfer equation. In the frame of the on-the-spot approximation applied, the population numbers are assumed to be homogeneous. The center of mass of the emitting region is chosen as reference point. The radiative transfer equations can then be solved analytically and we can put

$$I_{ij} = S_{ij} (1 - e^{-\tau_{ij}}) + I_{bg} e^{-\tau_{ij}}, \quad (3)$$

where  $I_{bg}$  represents the background radiation field. For  $j > i$  the optical depth  $\tau_{ij}$  and the source function  $S_{ij}$  are given by

$$\tau_{ij} = \kappa_{ij} R \quad (4)$$

$$\kappa_{ij} = \frac{h\nu}{c} B_{ij} \phi(\nu) \Delta n \quad (5)$$

$$S_{ij} = \frac{2h\nu^3}{c^2} \frac{n_j}{\Delta n} \quad (6)$$

$$\Delta n = \frac{g_j}{g_i} n_i - n_j, \quad (7)$$

$R$  denoting the path length along a given line of sight. For simplicity we assume the profile of the absorption coefficient to be a box profile with a thermal line width:

$$\phi(\nu) = \begin{cases} \frac{1}{\Delta\nu} & , |\nu - \nu_0| < \Delta\nu \\ 0 & , \text{else} \end{cases}, \quad (8)$$

$$\frac{\Delta\nu}{\nu} = \sqrt{\frac{2kT}{mc^2}}. \quad (9)$$

## 2.2. Geometry

The intrinsic numerical complexity which always arises in radiative transfer calculations when maser lines are involved, strongly recommends to use a geometry as simple as possible. In our case this applies even the more, since we have a large number of maser lines to deal with simultaneously. Hence we assume a homogeneous lens-shaped emission region. This choice of geometry and line profile allows an easy numerical calculation of the angle and line profile averaged intensity. As we are mainly interested in the qualitative effect of flattening, we approximate

the accurate integral (2) by averaging the intensity over thirty sections of equal solid angle. Varying the ratio of the two principal axis we study the influence of flattening on the observed intensity when the disk is seen edge on.

## 2.3. Atomic data

The Einstein A-values are calculated using Eqs. (3.1–3.3) of Brocklehurst (1970). For collisional excitation we use the approximate rate coefficients given by Eq. (16) in the publication of Gee et al. (1976). The probability for collisional ionization is  $q_{coll}(i) = \langle v Q_{coll,i}(v) \rangle$ , where we use the ionization cross sections of Burgess & Percival (1968), Eq. (37), and a Maxwellian velocity distribution at the respective temperature. The spectral photo ionization coefficients  $a_\nu$  are calculated as described by Seaton (1960). For the integrated photo ionization rate coefficients  $q_{ph}(i)$  we put

$$q_{ph}(i) = \int_{\nu_0(i)}^{\infty} \frac{4\pi}{h\nu} a_\nu J_\nu d\nu, \quad (10)$$

where  $J_\nu$  is the usual angle averaged intensity. In general, the source of ionizing radiation will be an O- or B-star. As a rough approximation, we replace  $J_\nu$  by a diluted black body radiation field at a temperature of 35000K. The rates for all the backward reactions are calculated by detailed balancing relations.

## 2.4. Method of computation

We calculate the population numbers for 250 energy levels. To solve the remaining set of nonlinear equations, we use a standard routine contained in the NAG Fortran library. An initial approximation is obtained by solving the set of linear equations describing the optically thin limit with  $\tilde{J}_{ij} = 0$ . We start the calculations with a cloud diameter of only  $10^5$ cm, for which the optically thin approximation certainly applies. The dimension of the model cloud is successively increased, always using the latest result as start value for the next model.

## 2.5. Radiation emitted by the maser region

The model we use is essentially made up to achieve qualitative theoretical insights, in particular to study under which physical conditions inversion of the population numbers occurs. As stated before the model rests on several very rough approximations. It is thus not very well suited for a detailed interpretation of observations. Nevertheless we believe that the self-consistent treatment of saturation effects justifies an attempt to compare our theoretical results with observational data. By Eqs. (2) and (3) we compute the intensity in the center of the spherical or ellipsoidal maser region in order to determine the occupation numbers. In contrast to this, for the comparison with observational data one needs to know the intensity at the edge of the emitting region, escaping into space. Staying strictly in the frame of our model assumptions implies to assume homoge-

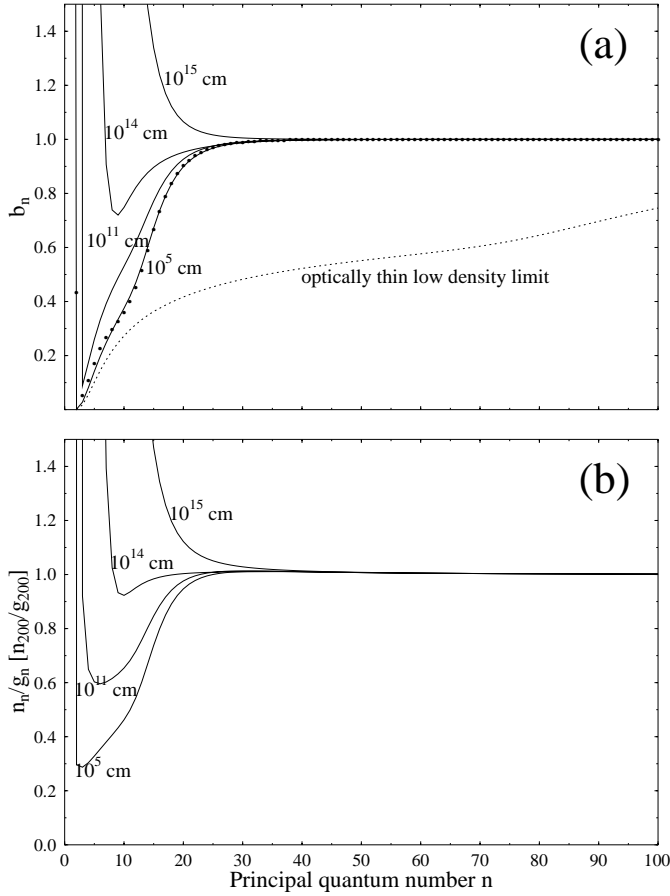


**Fig. 1. a:** solid lines:  $b_n$  coefficients for a spherical maser region with an electron density  $n_e = 10^8 \text{ cm}^{-3}$ , and a kinetic temperature  $T = 7500 \text{ K}$ . The radius of the sphere varies between  $R = 10^5 \text{ cm}$  and  $R = 10^{15} \text{ cm}$  (labels). For the smallest  $R$  our calculations are in good agreement with the optically thin Case A results of Storey & Hummer (1995) (dots). For large values of  $R$  radiative transfer becomes important (see text). The broken line shows the low density limit of the optically thin case ( $n_e = 10^2 \text{ cm}^{-3}$ ); here the quantum number from which on thermalization sets in is out of the plot range. **b:** same data as in **a** in a different representation (occupation numbers per quantum cell). In the chosen normalization a positive slope is equivalent with population inversion ( $\Delta n < 0$ ).

neous population numbers. Neglecting background radiation, we then find

$$I_{\nu,esc} = S_{\nu} (1 - e^{-\kappa_{\nu} l}), \quad (11)$$

where  $I_{\nu,esc}$  is the intensity radiated into space and  $l$  denotes the path length through the maser region, which is  $2R$  for a spherical region and  $2\sqrt{(\cos^2 \vartheta/a^2 + \sin^2 \vartheta/b^2)^{-1}}$  for a biaxial ellipsoid,  $\vartheta$  being the angle between the major principal axis and the line of sight. Eq. (11) represents exponential growth of the intensity with the path length, which is typical for completely unsaturated masers. If  $\kappa_{\nu}$  corresponds to the population numbers at the center of the emitting region, this overestimates the emitted intensity since saturation effects increase towards the edge. In the extreme case that the maser is saturated in the whole maser region the intensity is more likely to increase lin-

early along a given line of sight. Since the observations for MWC 349 show maser lines that are very likely to be affected by strong saturation effects (Thum et al. 1992), we estimate the emitted intensity by putting

$$I_{\nu,esc} = 2 I_{\nu,cen}, \quad (12)$$

$I_{\nu,cen}$  being the intensity in the given direction we obtain during our calculations at the center of mass.

### 3. Population structure and line intensities

#### 3.1. The effect of radiative transfer in the spherically symmetric case

The extent to which radiative transfer is involved in setting up the population numbers essentially depends on the column density of neutral hydrogen. Thus, for a given electron density and a given degree of ionization, the linear dimension  $R$  of our model cloud determines the strength of radiative transfer effects. Conventionally we give the population numbers of the hydrogen energy levels in terms of the  $b_n$  coefficients, which give the relative population numbers with respect to their thermal value (Boltzmann-Saha-equation). Thus the  $b_n$  are defined by

$$\frac{n_n}{n_e n_p} = \left( \frac{h^2}{2\pi m k T} \right)^{3/2} \frac{g_n}{2} e^{\frac{I_n}{kT}} b_n. \quad (13)$$

Fig. 1a shows the  $b_n$  coefficients calculated for an electron density  $n_e = 10^8 \text{ cm}^{-3}$  and a kinetic temperature of  $T = 7500 \text{ K}$ . The dimensions of the emitting region vary from  $R = 10^5 \text{ cm}$  up to  $R = 10^{15} \text{ cm}$ . For the smallest value of  $R$  our calculations are in perfect agreement with the calculations of Storey & Hummer (1995) (dots). The representation of the population numbers in terms of the  $b_n$  coefficients does not allow to identify population inversion directly, as a positive gradient of the  $b_n$  curve is not equivalent with  $\Delta n < 0$ . In Fig. 1b we therefore plot the population numbers per quantum cell ( $n_n/g_n$ ), normalized on  $n_{200}/g_{200}$ . In this representation, a positive gradient of the curve implies  $\Delta n < 0$ . Over a wide range of principal quantum numbers we find population inversion, indicated by the positive slopes for  $n \leq 35$ . In this region strong maser activity occurs especially in the  $\text{Hn}\alpha$ - and  $\text{Hn}\beta$  lines (cf. Fig. 8a, 8c). Obviously the main effect of radiative transfer is to produce high excitation in the low energy levels. Since the usual way of depopulation is a radiative cascade from the highly excited levels down to the ground state through the  $\alpha$  lines, we suspect that this cascade is interrupted when the low  $\alpha$  transitions become optically thick. In an optically thick line the radiative transitions are almost in detailed balance and each photon emitted during a radiative de-excitation process is being reabsorbed on the spot. Thus, as soon as the cascade reaches the upper level of an optically thick transition, the way further down gets blocked and the population numbers become bottled up in this level and the levels below. This supposition proves to be true as shown in Fig. 2, where for the three lowest  $\alpha$  transitions we plot the  $b_n$  of their upper level as a function of the respective optical depth. At a critical  $\tau$  the  $b_n$  rapidly increase

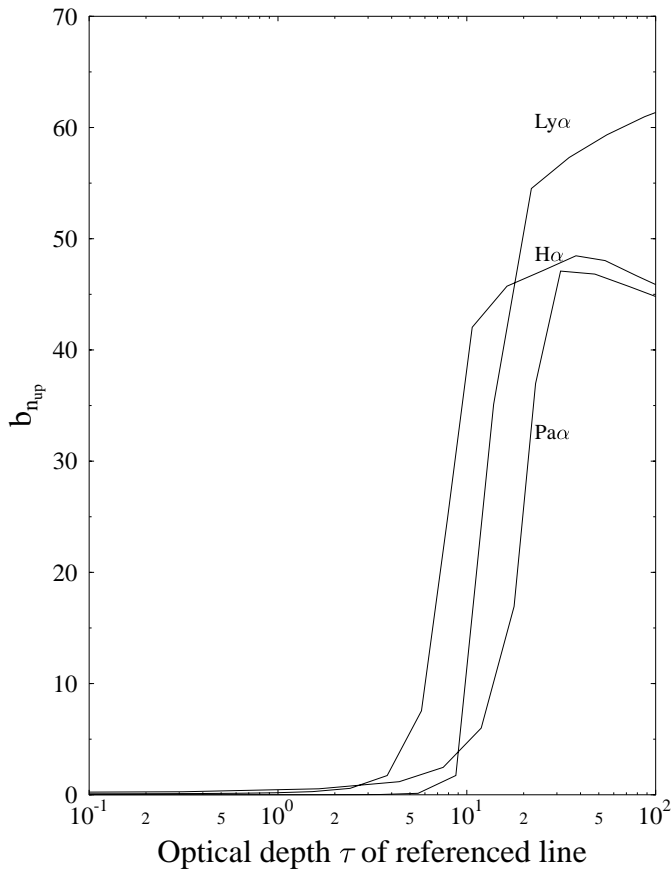


**Fig. 2.** As soon as the optical depth of one of the referenced lines reaches a critical value, the  $b_n$  coefficient of the corresponding upper level increases rapidly.

and then remain at a large value. The critical quantum number  $n_{crit}$ , separating  $Hn\alpha$  lines with positive and negative optical depth, advances to always increasing  $n$  as  $R$  increases, resulting in a successive raise of the whole  $b_n$  curve. When  $R$  exceeds a certain value population inversion vanishes completely. It is clear that this mechanism prevents the optical depth of the maser lines from falling below a bounding value, and as soon as  $n_{crit}$  reaches the upper level of a given maser transition, its optical depth will change sign and grow towards high positive values (Fig. 3).

### 3.2. Parameters for population inversion

One of the key questions for the evaluation of observational data is to find out for which sets of parameters the hydrogen masers work most efficiently in a given range of principal quantum numbers. Fig. 4 is a map showing the optical depth of the  $Hn\alpha$  lines (transitions  $n + 1 \rightarrow n$  in the  $n - \log(n_e)$  plane for  $R = 1.6 \cdot 10^{14} \text{cm}$  and  $T = 7500 \text{K}$ . There is only a narrow valley, where strong maser activity arises, i. e.  $\tau < -1$ . For  $\log(n_e) < 6.5$  all lines are optically thin and no significant maser action can occur. From the previous section we have learned that for each electron density  $n_e$  and each quantum number  $n$  there exists a critical radius  $R_{crit}$ , for which the tran-

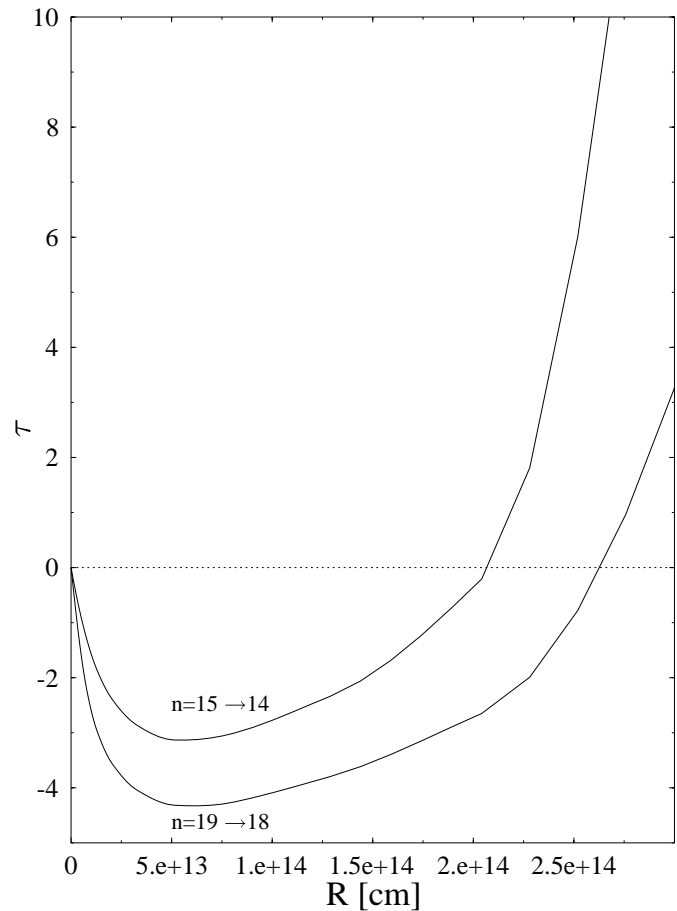


**Fig. 3.** Optical thickness  $\tau$  of the transitions  $n = 19 \rightarrow 18$  and  $n = 15 \rightarrow 14$  as a function of  $R$  ( $n_e = 10^8 \text{cm}^{-3}$ ). The saturation effects prevent the optical thickness from falling below a minimal value. At a critical value of  $R$ , population inversion ceases completely,  $\tau$  changes sign and grows rapidly.

sition  $n \rightarrow n - 1$  becomes optically thick ( $\tau > 1$ ). The upper boundary of the inversion valley is given by the pairs  $(n, n_e)$ , for which the fixed radius chosen to contour the optical depth is the critical radius. The lower density limit of the inversion valley occurs because at the given radius for too small values of  $n_e$  the column density of the maser transitions is insufficient for these lines to become strong maser lines ( $\tau < -1$ ). In the  $n$  direction strong maser emission in the  $\alpha$  lines occurs only for  $n \leq 45$ . The higher quantum states are thermalized by the balancing of collisional ionization and three body recombination. Of course, for smaller  $n_e$  this thermalization sets in only for higher quantum states, since the strength of the thermalizing processes is proportional to  $n_e^2$ . Especially for comparison with observational data it is interesting to plot the line integrated flux of the  $Hn\alpha$  lines escaping from the maser region as a function of the principal quantum number  $n$ . When crossing the inversion valley at a constant density value, a pronounced hump in the resulting curve marks the quantum number range where the line emission is amplified by stimulated emission (cf. Fig. 8a). Attention should be paid to the narrowness of the inversion region in the  $n_e$  direction, which certainly is part of the answer

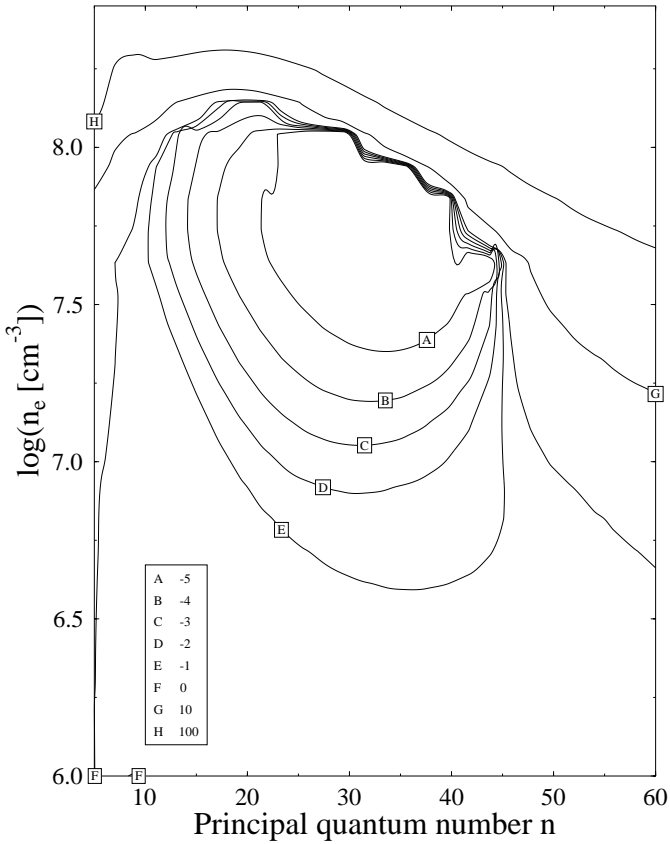


**Fig. 4.** Contour plot of the optical depth of the  $Hn\alpha$  lines (transitions  $n + 1 \rightarrow n$  in the  $n - \log(n_e)$  plane. The contour lines refer to the values of the optical depth  $\tau$  indicated in the box at the lower left. The region we refer to as *inversion valley* is bordered by the  $\tau = -1$  contour. ( $R = 10^{14}$  cm).

to the question, why we have knowledge of only one hydrogen maser object, MWC 349. This question implies the more general question, for which parameters  $(R, n_e)$  one should expect strong masers in the  $Hn\alpha$  lines at all.

To attack this question, we have extended our parameter space to values typical for common HII regions. In Fig. 5 we have set points for each pair  $(n_e, R)$ , for which we find  $\tau < -1$  for at least one of the  $\alpha$  lines. It is easy to explain the physics behind the lines bordering the resulting broad stripe in the  $\log(R) - \log(n_e)$  diagram. The lower boundary is constituted by the pairs  $(n_e, R)$  for which the most effective maser transition, i. e. the transition with maximum absolute value of  $|\kappa_{ij}|$ , becomes optically thick ( $\tau < -1$ ). From Fig. 1 we deduce that as long as the low  $\alpha$  transitions have only moderate optical depth, the overall shape of the  $b_n$  curve doesn't differ strongly from its optically thin limit. We thus search for the most efficient maser transition for the optically thin limit at each density value. For these we calculate the radius  $R_{inv}$  for which  $R_{inv} \kappa_{max} = -1$ . The points  $(\log(R_{inv}), \log(n_e))$  (thick dotted line in Fig. 5) perfectly fit the lower boundary of the inversion region. The upper border arises because, as we also learn from Fig. 1, for each density value population inversion vanishes for some critical  $R$ . We also mark the region in parameter space, that is accessible by standard cir-

cumstellar photoionization processes. The intersection of this stripe with the inversion region shows that, according to our model, one should find hydrogen masers in ultra compact HII regions of particular size and density ( $EM \geq 8 \cdot 10^7 \text{ cm}^{-6} \text{ pc}$ ). The densities in this vicinity are considerably smaller than those in the surrounding of MWC 349, which was the initial object under consideration. For these small densities, strong effects due to  $l$ -splitting of the energy levels arise (Storey & Hummer 1995). In view of this, it appears necessary to insure things don't change in principle when  $l$ -splitting is considered. As a first check, we plot the  $(\log(R_{inv}), \log(n_e))$  line using the optically thin results of Storey & Hummer (1995), who took into account the  $l$ -structure of the hydrogen levels (filled squares in Fig. 5). The line connecting these points is in perfect agreement with our calculations. We furthermore check whether we find the strongest maser activity in similar transitions for the two different models along this lower boundary line of the inversion region. It turns out that in the parameter region under consideration both models predict maser activity in a similar range of observable line transitions. The quantum number range over which population inversion is found is even larger in the case of low densities, since the collisional processes that quench population inversion in the high  $n$  vicinity are strongly weakened for low values of  $n_e$ . In the optically thin low density limit (Fig. 1) the collisionally thermalized part of the  $b_n$  curve is already out of the plotting range ( $n < 100$ ). While for  $n_e = 5 \cdot 10^7 \text{ cm}^{-3}$ ,  $R = 10^{14} \text{ cm}$  we have population inversion from  $H6\alpha$  up to  $H45\alpha$ , for  $n_e = 10^5 \text{ cm}^{-3}$ ,  $R = 4.3 \cdot 10^{17} \text{ cm}$  the inversion region ranges from  $H50\alpha$  up to  $H160\alpha$ . Since this range includes the most prominent recombination lines, and to our knowledge there is no observational evidence for the presence of hydrogen masers in UC HII regions, we consider our prediction to be worth becoming the subject of further investigation. We finally remark that the population structure also is influenced by the kinetic gas temperature. The reason is the strong temperature dependence of the rate coefficients for the thermalizing bound-free and bound-bound collisional transitions. The upper quantum number limit of population inversion due to collisional quenching moves toward lower quantum numbers with increasing temperature.

### 3.3. Ellipsoidal maser regions

In the following we discuss the effect of flattening on the maser radiation originating from a biaxial ellipsoid seen edge on, its flatness being characterized by the axis ratio  $b/a$ ,  $a$  denoting the major and  $b$  the minor principal axis of the ellipsoid.

Fig. 7 shows that for a given maser transition  $\kappa_\nu$  is a monotonically growing function of the length of the maser regions principal axis  $a$ , i. e. population inversion is strongest in the optically thin limit. The axis ratio  $b/a$  determines, at which value of  $a$  deviations from the optically thin limit arise. The smaller the  $b/a$ -ratio is, the larger this transition value will be. Starting with a spherical region ( $b/a = 1$ ), successive flattening at fixed  $a$  corresponds to jumping from one  $\kappa_\nu - a$ -curve in Fig. 7 to the next with ever decreasing  $b/a$ -parameter. According to Fig. 7,

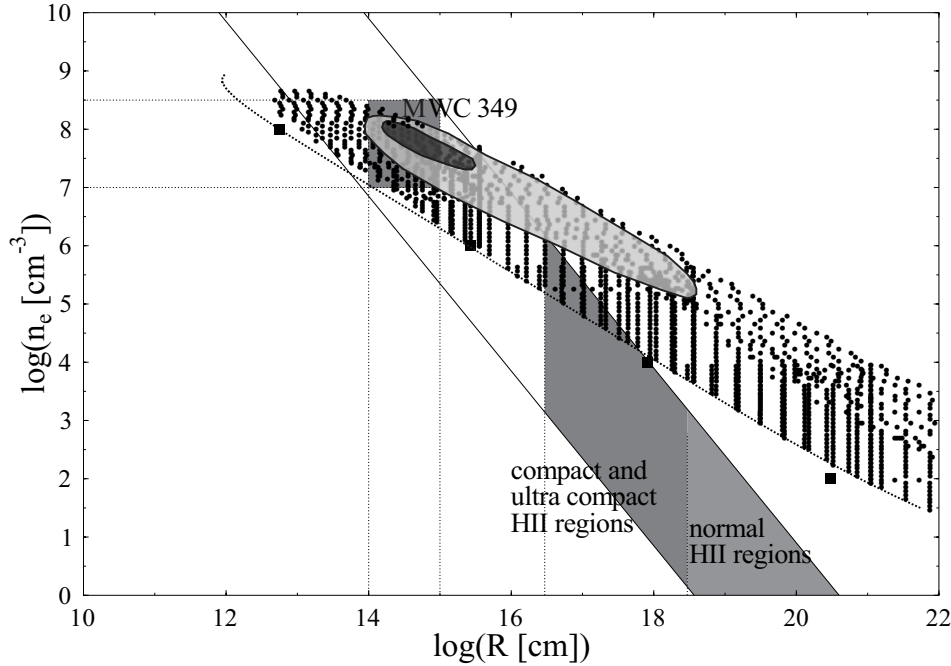


**Fig. 5.** Dots are set for each pair of  $(\log(n_e), \log(R))$ , for which  $\tau < -1$  for any  $\alpha$  line. The two solid lines mark the conventional Strömberg radius at given  $n_e$  for an O4 or B3 star, respectively. The stripe bordered by these lines is accessible by usual photoionization of circumstellar gas. For each density value  $n_e$  the thick dotted line identifies the radius  $R_{inv}$  for which the most effective maser line in the optically thin limit has an optical depth  $\tau = -1$ . The filled squares mark the corresponding  $R_{inv}$  calculated with the  $b_n$  values of Storey & Hummer (1995). All models are calculated for a kinetic temperature  $T = 7500\text{K}$ . The elliptical area marked with the light grey overlay shows the region where for  $\text{H}29\alpha$  we have  $\tau < -3$ . The embedded dark grey overlay marks the respective area for  $\text{H}19\alpha$ .

this leads to a decrease of  $\kappa_\nu$  until the optically thin limiting value is reached.

If we keep  $a$  fixed,  $|\tau_\nu|$  increases with decreasing  $\kappa_\nu$ , as for maser lines we have  $\kappa_\nu < 0$ . This means that the maser action becomes stronger the flatter the emitting structure is. In a flat emission region, the non-maser photons can escape along the minor axis direction, while the maser radiation is strongly focused to the disk plane. Hence, the adjustment of the population numbers becomes similar to the optically thin limit, and saturation effects are strongly reduced. For the calculations of the emitted radiation we thus use the completely unsaturated approximation (11). Fig. 6 shows that for ellipsoidal maser regions the maser hump in the  $F_\nu - n$ -plot is strongly overpronounced, according to the particular choice of the flattening parameter.

In the special case of MWC 349 the hypothesis has been set up, that the presence of maser lines was a consequence of the emitting region being located in a flat disk, i. e. that flattening was a necessary condition for maser action to arise. The fact that our model yields strong masers with moderate humps in the spherical case shows, that at least in the frame of our model this hypothesis does not hold. The weakness of the observed maser hump of MWC 349 even suggests the presence of strong saturation effects, which, as mentioned above, are strongly reduced in the flattened case and are strongest in the spherical case. In our opinion, this indicates that the coherent amplification path in the disk plane of MWC 349 cannot significantly exceed the vertical disk dimension.

For the general pictures of hydrogen masers in ionized disks this means, that they should be observable even face on, at least as long as the thickness of the disk is sufficient for effective maser amplification and there is no considerable line absorption by e.g. the lobes of an outflow perpendicular to the disk plane.

#### 4. Line intensities - comparison with observational data

For MWC 349 the amplification of the  $\text{H}n\alpha$  lines is well observed. The overall structure of the variation of the  $\alpha$  line flux with the principal quantum number has been studied by Thum et al. (1998). They find that the maser amplified lines form a bell-shaped hump standing out above the regularly decreasing emission. The observational data is shown in Fig. 8a (filled squares). From previous work, the parameters for the emitting region are estimated to be  $R \approx 10^{13} \dots 10^{14} \text{cm}$  and  $n_e \approx 10^8 \text{cm}^{-3}$  (Thum et al. 1994, Thum & Greve 1997). From Fig. 3 we know, that for these parameters in the spherical case the maser can be considered to be completely saturated, so again we restrict ourselves to spherically symmetric models. For the calculation of the absolute  $\text{H}n\alpha$  line fluxes we use the completely saturated approximation (12), putting

$$F_\nu = 2 I_{\nu, \text{cen}} \Delta\Omega \Delta\nu, \quad (14)$$

where  $I_{\nu, \text{cen}}$  is the intensity at the center of the sphere calculated in the frame of our on-the-spot approximation,  $\Delta\nu$  is the Doppler width at  $T = 7500\text{K}$ , and  $\Delta\Omega$  is the solid angle covered by the emitting region. Our model and especially this approximative approach to calculate the observable flux is too rough to use the fitting procedure as a method to determine  $\Delta\Omega$ , so it cannot serve as an independent distance indicator. For each pair  $(R, n_e)$  in the parameter space shown in Fig. 5, the logarithms of the calculated  $\text{H}n\alpha$  line fluxes are thus only shifted by their mean deviation from the observed fluxes. Then the mean square deviation between observations and shifted calculations is being calculated and the whole parameter space is being scanned for the pair  $(R, n_e)$  for which this error measure takes the minimum value. We find best coincidence for  $n_e = 8.9 \cdot 10^7 \text{cm}^{-3}$  and  $R = 5.8 \cdot 10^{13} \text{cm}$  (Fig. 8a). For comparison it is interesting to note that the horizontal dimension of the disk of MWC

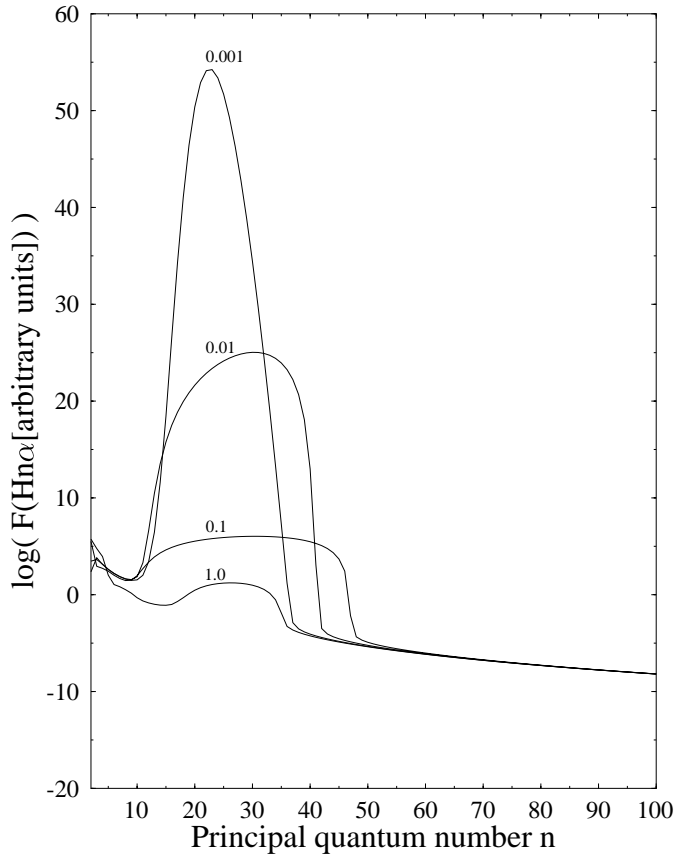


**Fig. 6.** Impact of flattening on the line integrated  $\alpha$ -line fluxes. The labels denote the axis ratio  $b/a$ . The stronger the flattening of the maser regions is, i. e. the smaller  $b/a$ , the more saturation effects are being suppressed, and the maser hump gets more and more overpronounced. ( $\log(n_e [\text{cm}^{-3}]) = 7.5$ ,  $\log(a [\text{cm}]) = 14$ )

349 is estimated from observations to be about  $10^{15} \text{cm}$  (Leinert 1986). Our spherical best fit maser region thus is small enough to fit into this disk. The fact that we do not necessarily need to take into account the flatness of the disk of MWC 349 may be regarded as a hint that hydrogen masers may also be observed in dense disks that are not seen edge on, in contrast to the general opinion that this was a necessary condition for strong maser lines to arise.

Besides the absolute  $Hn\alpha$  line fluxes, two other observational quantities have been checked against optically thin recombination line models. The Paschen decrement calculated using the Case B model by Storey & Hummer (1995) has been shown to be compatible with the observational data collected by Thum & Greve (1997), and can even be used as a density discriminator. Taking into account the Paschen transitions from Pa8 up to Pa28, Thum & Greve derive an electron density of approximately  $10^8 \text{cm}^{-3}$ . In a more recent publication, Thum et al. (1998), the attempt to reproduce the observed ratio of the line integrated fluxes of  $\beta$ - and  $\alpha$ -lines with a common upper level using the same model failed. While the observations show a steep decrease of the  $\beta/\alpha$ -ratio, the theoretical Case B

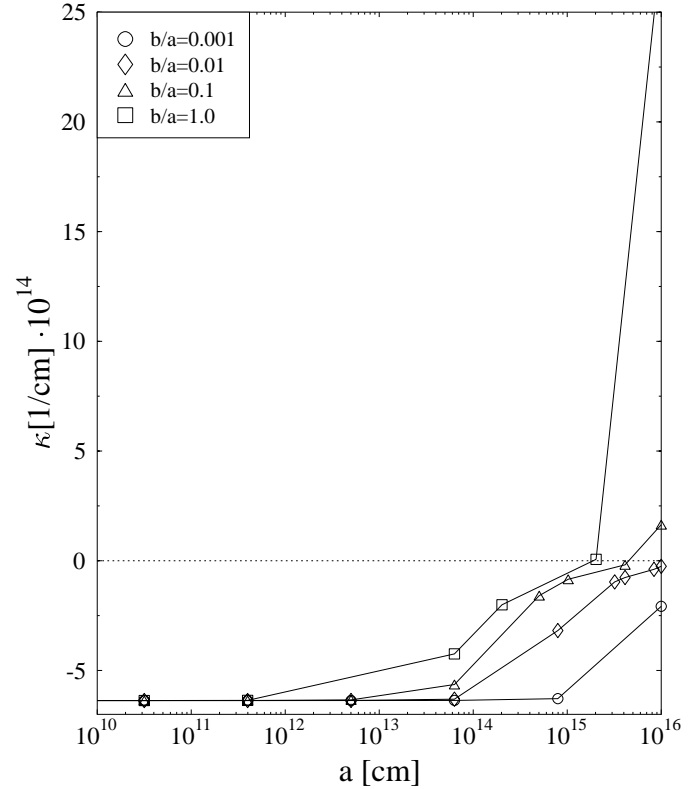


**Fig. 7.** Variation of the absorption coefficient of the transition  $n = 19 \rightarrow 18$  with the major axis of the maser region  $a$ . The different curves correspond to different values of the ratio of the minor and major principal axis,  $b/a$ . ( $\log(n_e) = 7.5$ .)

calculations lead to an essentially flat curve. We compare these two findings to the results of our model calculations.

On the one hand, we wish to find out if a density estimation using our calculated Paschen decrement and the observational data presented by Thum & Greve (1997) yields a result compatible with the evaluation using an optically thin recombination line model.

Following Thum & Greve (1997), we correct the observed Paschen line fluxes for interstellar extinction, using a reddening law  $A_\lambda \propto \lambda^{-1.85}$  with  $A_V = 10 \text{mag}$  (Cohen et al. 1985). For the parameter range explored, we again find best coincidence for a density  $n_e = 8.9 \cdot 10^7 \text{cm}^{-3}$ , which, in view of the rough approximation in both approaches can be considered as a perfect coincidence with the findings of Thum and Greve.

On the other hand, we wish to find out if the radiative transfer effects included in our model can help to reproduce the slope of the  $\beta/\alpha$ -ratio. The set of parameters for which we can approximately fit these data is  $n_e = 2.2 \cdot 10^8 \text{cm}^{-3}$  and  $R = 3.9 \cdot 10^{13} \text{cm}$  (dotted line in Fig. 8c). As by none of the above methods the parameters of MWC 349 can be determined to a precision of more than an order of magnitude, these parameters still have to be considered as to be in good agreement with the results for the other observational quantities. Moreover, the dotted lines in Fig. 8a and Fig. 8b show, that for this set of parameters the the Paschen decrement is well reproduced, and the fit for the

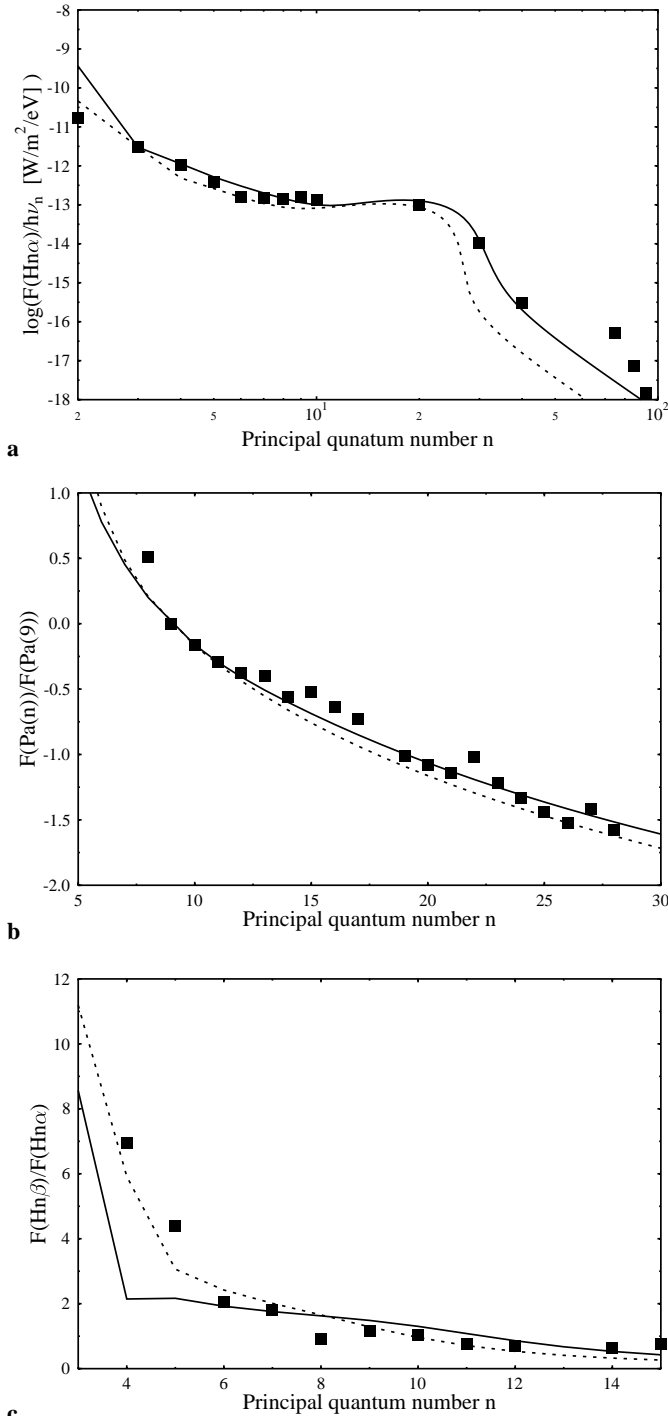


**Fig. 8a–c.** Best fit for the line integrated flux of the  $\alpha$ -lines **a**, the Paschen decrement **b** and the  $\beta/\alpha$ -ratio **c**. Observational data (filled squares): **a** and **b**: Thum et al. (1998) (corrected for interstellar extinction by Thum et al. (1998)), **c**: Thum & Greve (1997) (as not yet corrected by these authors, we have applied the reddening law they suggest in Thum & Greve (1997), i. e. we use  $A_\lambda \propto \lambda^{-1.85}$  with  $A_V = 10 \text{ mag}$ ). In **a** the photon flux  $F_\nu/h\nu$  is used in order to emphasize the maser hump. Solid lines: fit for  $n_e = 8.9 \cdot 10^7 \text{ cm}^{-3}$ ,  $R = 5.8 \cdot 10^{13} \text{ cm}$ . Broken lines: fit for  $n_e = 2.2 \cdot 10^8 \text{ cm}^{-3}$ ,  $R = 3.9 \cdot 10^{13} \text{ cm}$ .

$\alpha$ -lines is acceptable, except for the high quantum numbers. In contrast to this, for  $n_e = 8.9 \cdot 10^7 \text{ cm}^{-3}$  and  $R = 5.8 \cdot 10^{13} \text{ cm}$  (the parameters that fit the Paschen decrement and the  $\alpha$ -lines) the  $\beta/\alpha$ -ratio is only poorly reproduced. The curve remains essentially flat because at these parameters both the  $\alpha$ - as well as the  $\beta$ -lines are optically thin. For  $n_e = 2.2 \cdot 10^8 \text{ cm}^{-3}$  and  $R = 3.9 \cdot 10^{13} \text{ cm}$ , the  $\alpha$ -lines already tend to become optically thick, while the  $\beta$ -lines still remain optically thin, the  $\alpha$ -line photons then being trapped while the  $\beta$ -line photons can escape. When attempting to fit all three observational quantities simultaneously, we end up with the parameters fitting the  $\beta/\alpha$ -ratio.

The successive analysis of several groups led to an always improving picture of MWC 349, putting always tighter constraints on the density and spatial extent of the masing region. We suggest to put a further restriction on the allowed parameters by requiring that for H19 $\alpha$  strong maser action is present, i. e.  $\tau < -3$ . This condition will certainly apply to the case of MWC 349, as for this object amplification of the  $\alpha$ -line peaks at about  $n = 19$ . The area in parameter space for which, according to our calculations, the above condition holds, is marked by the dark grey elliptical overlay in Fig. 5.

Previous authors repeatedly have speculated that the different maser lines are emitted under different physical conditions. E. g. Thum et al. (1994) propose that each transition is being emitted near its critical density above which collisions are found to quench maser activity for the respective transition in standard Case B theory (Walmsley 1990). The different maser transitions then are attributed to distinct spots in the circumstellar disk of MWC 349, their density varying by almost an order of magnitude. Strelitski et al. (1996) point out that each transition is more likely emitted at its maximum gain density, i. e. at the density for which it reaches its minimal absorption coefficient. Using a disk model by Hollenbach et al. (1994) they locate the different transitions at positions in the disk with distances from the disk center that even vary by three orders of magnitude. Their model hence assumes different amplification path length and electron densities for different line transitions that differ tremendously. In Fig. 5 we have inserted two contours that mark the parameters where for the 19 $\alpha$  transition (dark contour) and the 29 $\alpha$  transition (light contour)  $\tau < -3$ . The 19 $\alpha$ -contour is completely embedded in the 29 $\alpha$ -contour. Thus, over the whole parameter range for which H19 $\alpha$  is strongly maser amplified the H29 $\alpha$  maser is working at high efficiency, too. The same is true for other lines. The picture that at a given density only one single maser transition can operate efficiently can not be confirmed, according to our calculations.

## 5. Conclusion

Applying a simple on-the-spot approximation on the sophisticated problem of the adjustment of the hydrogen population numbers, allowed us to obtain new insight into the mechanisms that give rise to the appearance and disappearance of population inversion in atomic hydrogen. Our model is the first to account for the solution of statistical equations and radiative transfer

equations simultaneously. We have shown that the influence of radiative transfer is not at all negligible, as it is the driving force in quenching population inversion, at least at a temperature of  $T = 7500\text{K}$ .

We have been able to show that strong hydrogen masers are not restricted to such special objects like MWC 349 but that they might be found in a certain class of ultra compact HII regions as well. The fact that to our knowledge there is no observational evidence for the occurrence of hydrogen masers in these objects, gives rise to new curiosity and theoretical as well as observational effort.

In the frame of our simple model, there also is no need for a masing disk to be seen edge on. We have furthermore shown that it is not appropriate to attribute certain line transitions to a typical density. These findings rule out two fundamental assumptions that have been believed to be valid in general. Circumstellar disks around hot stars now seem to be even more promising candidates to find new objects that show maser activity in the transitions of atomic hydrogen, since the maser hump should be present even for a disk seen face on if its thickness and density match a pair  $(R, n_e)$  for which strong maser action is indicated in our diagnostic plot. The maser lines then are perfectly suited to probe the physical conditions in the disk.

Our model is the first one to represent the steep drop of the  $\beta/\alpha$  ratio measured for MWC 349. We could also derive far tighter restrictions for the area of parameter space that may be suitable for the masing disk of MWC 349. As soon as the ISO observations of MWC 349 (Thum et al. 1998, Thum & Hengel 2000) are reduced completely, we plan to apply our method to

all the series of hydrogen that will be available then. This should help to refine our general picture of MWC 349.

*Acknowledgements.* We would like to thank Clemens Thum from IRAM for many valuable comments and helpful discussions.

## References

- Brocklehurst M., 1970, MNRAS 148, 417  
 Burgess A., Percival I. C., 1968, Adv. Atom. mol. Phys. 4, 109  
 Chandra S., Kegel W. H., Albrecht M. A., et al., 1984, A&A 140, 295  
 Cohen M., Biegging J. H., Dreher J. W., et al., 1985, ApJ 292, 249  
 Gee C. S., Percival I. C., 1976, MNRAS 175, 209  
 Hollenbach D., Johnstone D., Lizano S., et al., 1994, ApJ 428, 654  
 Kegel W. H., 1979, A&AS 38, 131  
 Köppen J., Kegel W. H., 1980, A&AS 42, 59  
 Leinert C., 1986, A&A 155, L6  
 Martín–Pintado J., Bachiller R., Thum C., et al., 1989, A&A 251, L13  
 Seaton M. J., 1960, Reports on Progress in Physics XXIII, 313  
 Storey P. J., Hummer D. G., 1995, MNRAS 272, 41  
 Strelitski V. S., Ponomarev V. O., Smith H. A., 1996, ApJ 470, 1118  
 Thum C., Greve, A., 1997, A&A 281, 161  
 Thum C., Hengel C., 2000, in preparation  
 Thum C., Martín–Pintado J., Bachiller R., 1992, A&A 256, 507  
 Thum C., Strelitski V. S., Martín–Pintado J., et al., 1994, A&A 283, 582  
 Thum C., Martín–Pintado J., Quirrenbach A., et al., 1998, A&A 333, L63  
 Walmsley, C. M., 1990, A&AS 82, 201